Supplementary Information

Crystal structure analysis

Table S1: Crystal data and structure refinement of compound **I**.

Structural parameters	**$(C_5H_8N_3)_2[CoCl_4(C_5H_7N_3)_2]$**
Empirical formula	$C_{20}H_{30}Cl_4CoN_{12}$
Formula weight (g.mol^{-1})	639.29
Wavelength (Å)	0.71073
Temperature (K)	125.8(3)
Crystal system	Triclinic
Space group	P-1
***a* (Å)**	7.6349(7)
b (Å)	8.9698(10)
***c* (Å)**	11.0037(12)
α (°)	106.884(10)
β (°)	97.904(9)
γ (°)	110.288(9)
V (Å^3)	652.10(13)
Z	1
Calculated density (mg/m^3)	1.628
Absorption coefficient (mm^{-1})	1.105
F(000)	329
Crystal size (mm^3)	0.3 x 0.3 x 0.3
θ range for data collection (°)	2.950 to 24.994
h,k,l range	-8<=h<=9 -10 ≤ k ≤10 -13 ≤ l ≤ 12
Reflections number	**2278**
Absorption correction	Semi-empirical from equivalents
Transmission factors	T_{min}= 0.75630, T_{max}=1.00000
Number of parameters	191
Goodness of fit (F^2)	1.044
R_1	0.0671
wR_2	0.1606

Largest diff. peak and hole (e.Å^{-3})	1.532 and -0.891

Table S2: Bond distances surrounding the metal center.

Bonds	Distances
Co–N1	2.246(3)
Co–Cl1	2.5089(9)
Co–Cl2	2.4528(9)

Table S3: Hydrogen-bond geometry (Å, °) of compound **I**.

D—H···A	d(D—H)(Å)	d(H···A)(Å)	d(D···A)(Å)	∠D—H···A(°)
N2–H2N···N6^{i}	0.92(2)	2.23(4)	3.130(4)	165(3)
N2–H2N···Cl1 (intra)	0.92(3)	2.32(3)	3.141(4)	149(3)
N5–H5N···Cl2	0.92(4)	2.32(3)	3.190(4)	158(3)
N5–H5N···N3^{ii}	0.92(3)	2.05(3)	2.945(4)	168(5)
N4–H4N···Cl1	0.92(4)	2.70(4)	3.300(3)	124(3)
N4–H4··· Cl2	0.92(4)	2.69(5)	3.450(4)	141(3)
N2–H2N···Cl1 (intra)	0.93	2.62	3.160(4)	117

Symmetry codes: (i) x,y,-1+z; (ii) x,y,1+z; (iii) 2-x,2-y,-z.

- ***Hirshfield surface***

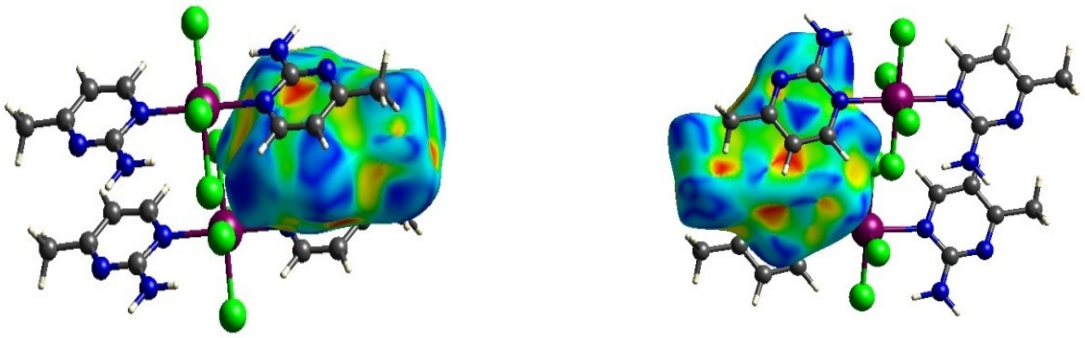

(c) **(d)**

Figure S1: (c), (d) 3D Hirshfield surface plot of front and back views of the aromatic electrostatic effect.

- *Powder X-Ray diffraction*

The PXRD analysis is employed to verify the complex's bulk purity. It can be inferred, from the experimental and the calculated diffractograms (Figure S2), the presence of distinctive characteristic peaks of the complex without any traces of other impurity peaks.

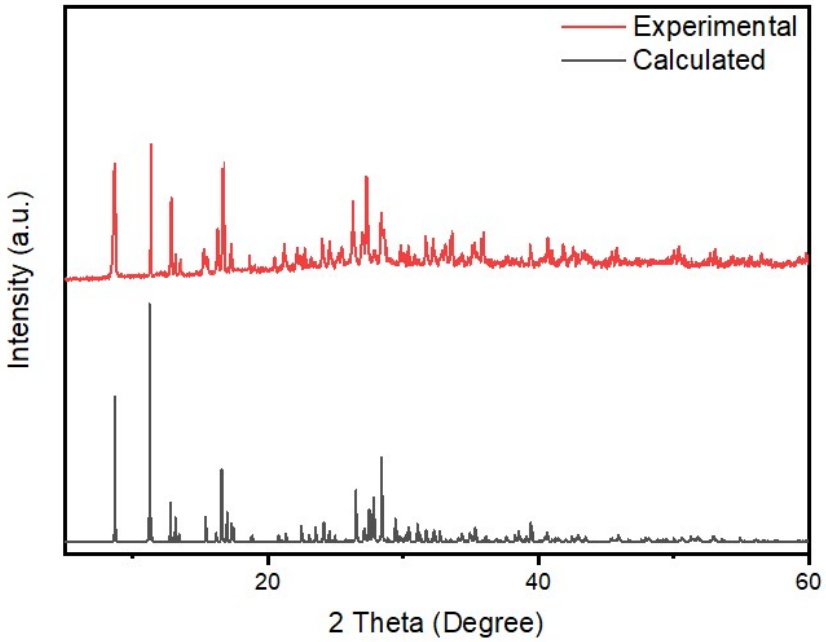

Figure S2: Experimental (red line) and calculated (black line) of powder XRD of compound **I**.

Analysis of the infrared absorption

Based on **Figure S3**, the spectral range from 500 to 1700 cm^{-1} corresponds to the low-frequency region. From 500 to 1220 cm^{-1}, there was the detection of bands relative to γ(C–NH_2), ν(C–C) and δ(C–C). Stretching vibration modes ν(C=C) and ν(C=N) of the aromatic ring are displayed at 1348 cm^{-1}, 1377 cm^{-1} and 1465 cm^{-1}. The intense bands found at 1628, 1671 cm^{-1} are related to δ(NH) relative to NH_2 and NH^+ groups. The high-frequency region belongs to the area ranging from 2700 cm^{-1} to 3500 cm^{-1}. The partial superposition of the valence vibrations of N–H^+, N–H_2, C–H, and NH_2^+ are noticed at 2800 cm^{-1}, 3170 cm^{-1}, 3180 cm^{-1}, and 3300 cm^{-1}, respectively.

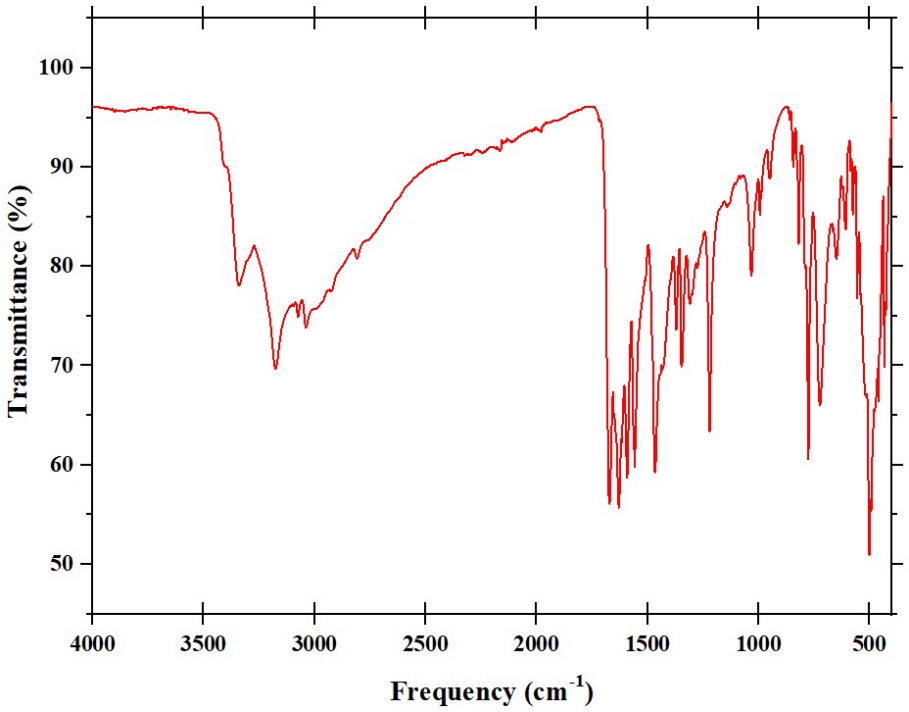

Figure S3: Infrared absorption spectrum of compound **I**.

Table S4: Vibrational modes of the organic parts of compound **I**.

Low frequencies (500-1700 cm^{-1})	
γ (C-NH_2)	500-1220 cm^{-1}
ν (C-C)	500-1220 cm^{-1}
ν (C=N)	1377 cm^{-1}
N-H_2	1628 cm^{-1}
N-H^+	1671 cm^{-1}
High frequencies (2000-4000 cm^{-1})	
N-H^+	2800 cm^{-1}
N-H_2	3170 cm^{-1}
C-H	3180 cm^{-1}
NH_2^+	3300 cm^{-1}
O-H	3343 cm^{-1}

Thermal analysis

It can be seen from this measurement that the complex has three thermal decomposition stages (**Fig. S4**). The main weight loss can be attributed to the decomposition of the discrete amine groups with the two chlorine atoms, possessing the longer distances between Cl and Co metal, are removed to support the charge neutrality (calc: 45%, theo: 44%). The second stage corresponds to the degradation of the two remaining chlorines (Cl2 and Cl2a), which possess the shortest distances relative to the metallic center than the others (observed: 10%, calcd. 11.1%). The departure of the Ampym ligands coordinated to the metal ion marks the final phase of the compound's decomposition (found: 32%, calcd. 34.13%). The last transformation results in the creation of cobalt oxide as a final product (theoretical value, 11.73%), accompanied by an exothermic peak on the DTA curve detected at 750°C.

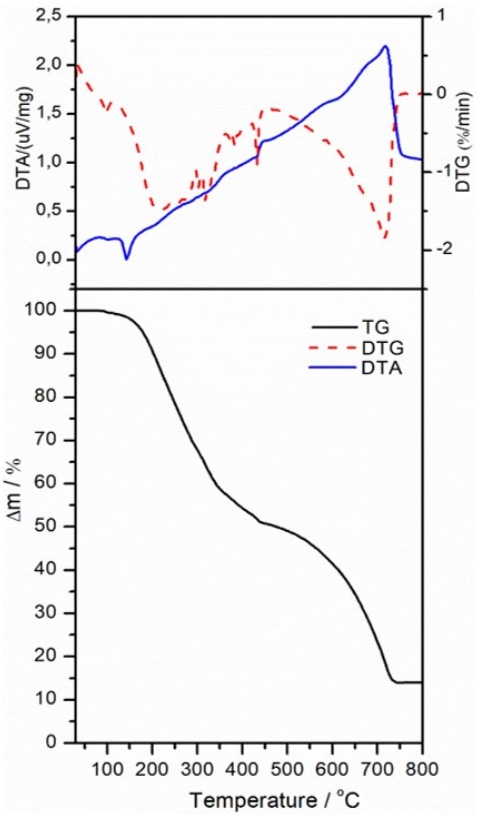

Figure S4: Thermal analysis DTA/TG of compound **I**.

UV-visible spectroscopy

Based on the Kubelka–Munk function, the collected reflectance spectrum was transformed into an absorption spectrum using the following relationship: $F(R) = (1 - R)^2/2R$, where R is the reflectance of the sample. **Figure S5** shows three bands with high intensities in the range below 400 nm and a large one with lower intensity located in the visible region. The π-π* electronic transitions are assigned to the two bands at 200 and 249 nm. However the third one, esteemed at 347 nm, is ascribed to the n-π* from the ligand to metal charge transfer transition (LMCT). [1] The visible region is dominated by highest energy transition $^4T_1g(F) \rightarrow {}^4T_{1g}(P)$ specific for Co d-states, the band consists of more than one band where a shoulder is found. There are two probable explanations for this specific finding. The first one, the shoulder in the band relatively weak in intensity is a two-electron transition related to $^4T_{1g}(F) \rightarrow {}^4A_{2g}$ transition. This transition looks to be fairly near to the more intense $^4T_{1g}(F) \rightarrow {}^4T_{1g}(P)$ transition, it is a like hood that the $^4T_{1g}(F) \rightarrow {}^4A_{2g}$ band could be covered by the $^4T_{1g}(F) \rightarrow {}^4T_{1g}(P)$ band.[2] The second explanation is based on Tanabe Sugano diagram for a d^7 ion of octahedral cobalt (II), where the energy ratio ν_3 and ν_2 of the two transitions are known.

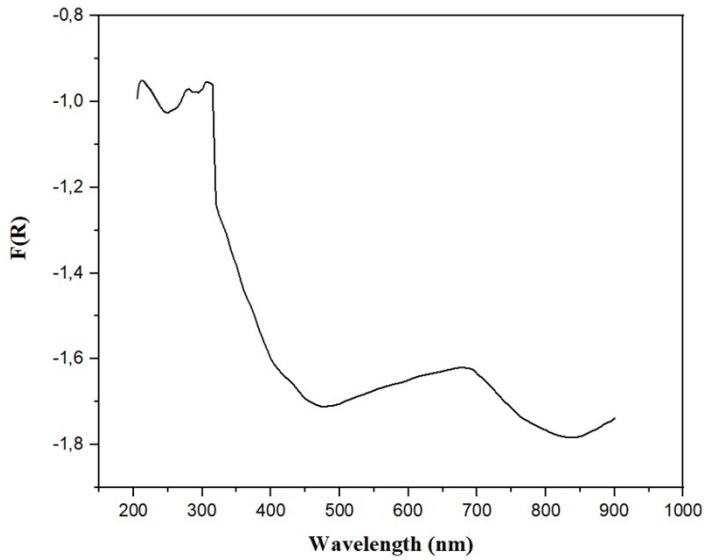

Figure S5: Optical spectrum of compound **I**.

From the Tauc plots, the band gap energy can be determined. The corresponding graph is constructed applying the Tauc relation, which links the absorption coefficient (α) with the gap energy value: $\alpha h\nu = A(h\nu - E_g)^m$, where *h* is the Planck's constant, *A* is a constant and the exponent "*m*" is a constant describing the gap transition's characteristics (m = 2 or ½). According to **Figure S6**, the optical band gap energy value is around 3.4 eV.

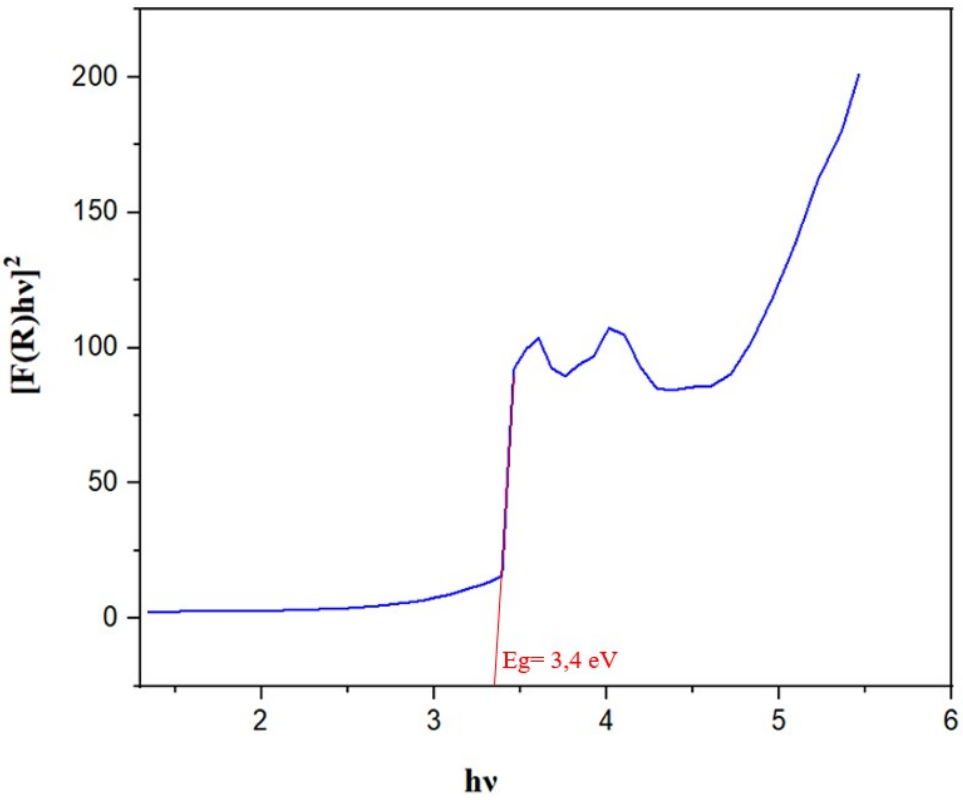

Figure S6: Optical band gap energy of compound **I**.

- ***Periodic DFT calculations***

Figures S7a and **S7b** shows the DOS and PDOS of $(C_5H_8N_3)_2[CoCl_4(C_5H_7N_3)_2]$ structure, respectively. The valence band maximum is mostly composed by p-states of N and C atoms from the complex with a minor proportion of d-states of Co and p-states of Cl atoms (**Fig. S7c**). There is an overlap between the p-states of Cl and d-states of Co, that corroborates the interaction between Co and Cl atoms in the formation of the complex. The first band that appears in the gap is centered

around 2.8 eV with a major proportion of p-states of N and C atoms (**Fig. S7d**). However, the band around 3.3 eV is dominated by the d-states of Co (**Fig. S7d**). Thus, the presence of Co in the structure plays a crucial role in electronic transitions by the presence of empty d bands in the gap.

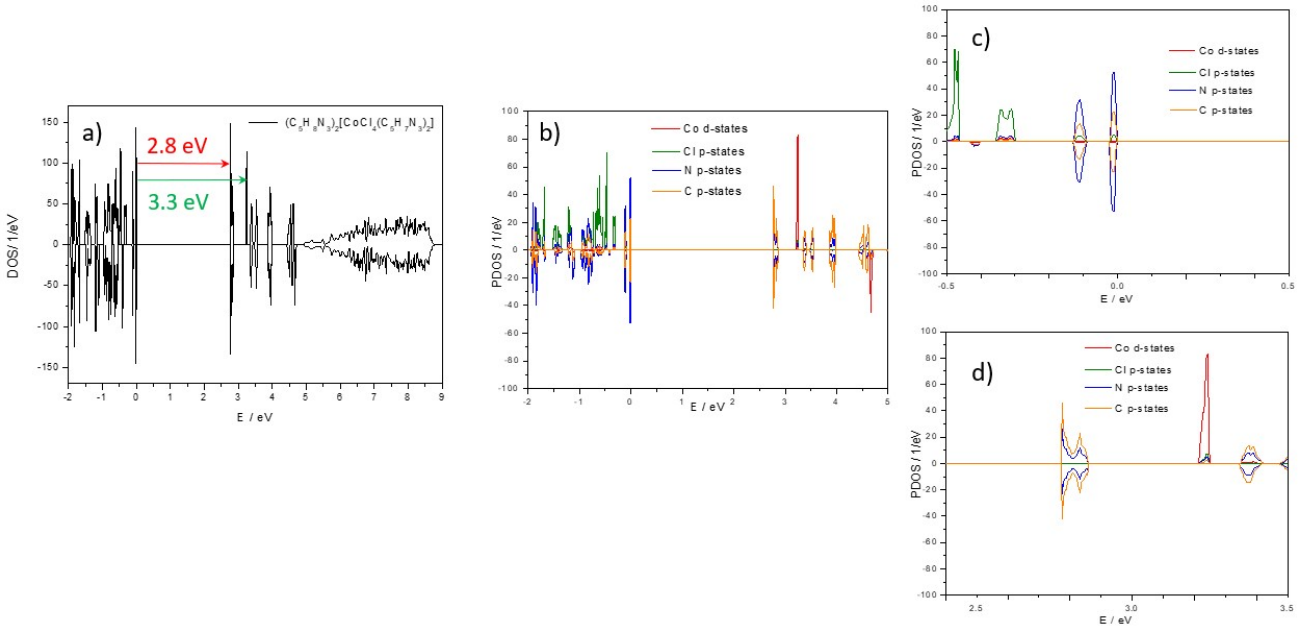

Figure S7. DOS (A) and PDOS (B) of $(C_5H_8N_3)_2[CoCl_4(C_5H_7N_3)_2]$.

Analysis of the slow magnetic relaxation

The extraction of the relaxation times was performed using a modified Debye model accounting for two independent relaxation processes given by the formula

$$\chi(\omega) = \chi_S + \sum_{k=1}^{K} \frac{\chi_{Tk} - \chi_{Tk-1}}{1 + (i\omega\tau_k)^{1-\alpha_k}} \quad , \qquad \textbf{(ES1)}$$

where χ_S is the overall adiabatic susceptibility, χ_{Tk} is the isothermal susceptibility, $\omega = 2\pi f$ is the angular frequency, τ_k is the relaxation time for k-th relaxation process, α_k describes the distribution of relaxation times of k-th relaxation process, and K defines the number of relaxation channels. The

real and the imaginary parts of **Eq. ES1** were extracted by a fitting script in MATLAB and fitted to the experimental data of χ' and χ'' simultaneously.

A complete formula that would include all possible relaxation mechanisms (field-dependent Raman described by Brons-Van Vleck model, direct, Orbach, and QTM process), if they coexist in one relaxation channel, can be written as

$$\tau^{-1} = \tau_{BVV}^{-1} + \tau_{D}^{-1} + \tau_{ORB}^{-1} + \tau_{QTM}^{-1} = \tau_{ZF}^{-1}\frac{1+dH^2}{1+eH} + ATH^4 + \tau_0^{-1}e^{-\frac{U_{eff}}{k_BT}} + \frac{D_1}{1+D_2H^2}, \quad \textbf{(ES2)}$$

where τ_{ZF}^{-1} represents a zero-field Raman process $\tau_{ZF}^{-1} \equiv \tau_{R}^{-1} = CT^n$, with characteristic constants A,

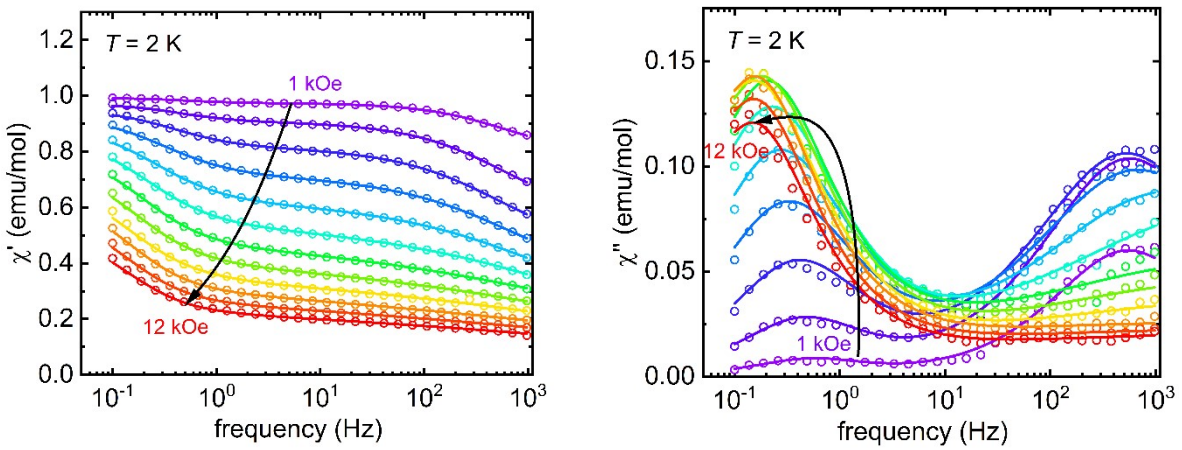

Figure S8: Frequency dependence of real (left panel) and imaginary (right panel) components of AC susceptibility of **I** measured at different applied DC fields at 2 K in the frequency range 0.1 Hz – 1 kHz including the fit of the modified Debye model with two relaxation channels.

C, D_1, D_2, d, e, τ_0, and U_{eff} for each process.

References

[1] G. G. Mohamed and Z. H. A. El-Wahab, “Mixed ligand complexes of bis(phenylimine) Schiff base ligands incorporating pyridinium moiety: Synthesis, characterization and antibacterial activity,” *Spectrochim. Acta - Part A Mol. Biomol. Spectrosc.*, vol. 61, no. 6, pp. 1059–1068, 2005, doi: 10.1016/j.saa.2004.06.021.

[2] L. F. Chibotaru and L. Ungur, “Ab initio calculation of anisotropic magnetic properties of complexes. I. Unique definition of pseudospin Hamiltonians and their derivation,” *J. Chem. Phys.*, vol. 137, no. 6, p. 64112, Aug. 2012, doi: 10.1063/1.4739763/72538.